Power optimisation of a rogue-wave energy device in a contraction

Onno Bokhove[1] and Harvey Thompson[2]

Abstract—We consider optimisation of a wave-energy device placed in a contraction consisting of unidirectional wave-induced buoy motion coupled to a tubular electromagnetic generator. First, optimisation of the generator is achieved by using three induction coils instead of one. Second, geometric optimisation is explored for two contraction-shape parameters. Finally, we discuss the advantages of using nonlinear Boussinesq-type wave models and their coupling to the buoy with an inequality constraint.

I. INTRODUCTION

There are a wide variety of devices that can harness wave energy, which can be placed in specific locations such as in the open ocean, in coastal waters or on the coast. We consider a niche wave device that is perhaps best embedded as part of the coastline, in particular either on a larger scale in a breakwater or on a smaller scale as part of a dock. The device consist of a buoy shaped and fit to move uni-directionally with and against gravity in a contraction. This contraction is used to enhance the wave action onto a buoy which is in turn driving a tubular permanent-magnet generator of the power. The device combines features of the tapered channel or Tapchan device (in which waves are raised to spill into a higher reservoir), heaving wave buoys with a linear and vertically-aligned generator, and the oscillating water column (OWC) driving Wells' wind turbines placed in a breakwater or on the open sea [12]. In the absence of the contraction and movement along a vertical wall, our device resembles the Berkeley wedge wave device [20] but that device has a sliding rail and sliding non-tubular linear motor. Alternatively, our device can be placed in a floating contraction geometry at sea, as in the device of Yu et al. [23], in which a contraction geometry is used to enhance the forces on 2×2 OWCs on its slanted side walls. The advantage of our device is the direct conversion of wave energy via buoy motion into electrical power. Our device was inspired by the rogue-wave amplification in the "bore-soliton-splash" [5].

A rendering of the device is given in Fig. 1. The dynamics involved has three integrated aspects: the waves coming from the sea enter the contraction, wherein a buoy is moving uni-directionally, and a main magnet attached to this buoy travels through tubular coils to generate the energy. A complete wave-to-wire mathematical model has been derived and partially explored in a series of papers [5], [6], [7]. Particular in that derivation is that the entire conservative part of the model can be derived from one variational principle,

with embedded therein the full two-way couplings between wave dynamics and buoy motion as well as integrated buoy motion and tubular electromagnetic power generation. The latter buoy-generator integration involves an analytic reduction of the three-dimensional Maxwell's partial differential equations in a symmetric, cylindrical configuration to two ordinary differential equations for the dynamics of charge and current in a single induction coil. Whereas the wave dynamics was modelled with nonlinear potential flow or Boussinesq-type partial differential equations and the buoy motion by two ordinary equations for the position and speed of the buoy. The advantage of this Boussinesq-type wave modelling over Navier-Stokes hydrodynamics is its speed and accuracy for the fast inertial wave motions involved. Such approximations are well-explored and customary in the wave dynamics community but have barely been explored in conjunction with (the optimisation of) wave-energy devices. Preliminary numerical investigations were undertaken by us based on a linear shallow-water version of this full wave-to-wire model. Here our aim is to optimise the power output of the device.
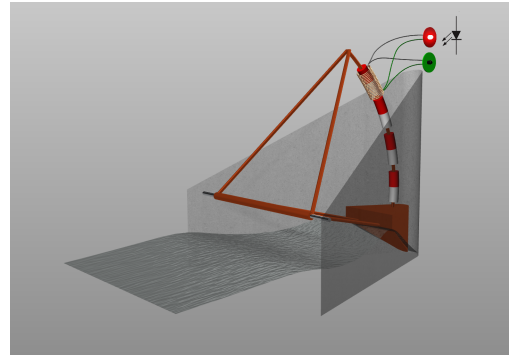
(a) Rendering of the device in the contraction with PTO, loads and incoming waves (courtesy Wout Zweers).
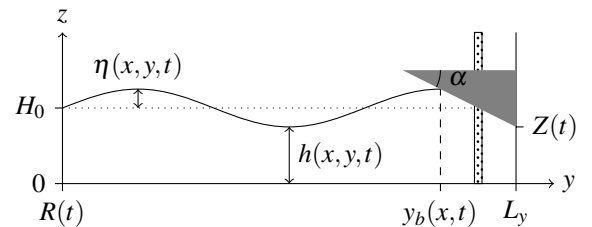
(b) Side view with buoy constrained to move vertically.

Fig. 1: Sketch of the wave-energy device (taken from [7]).

Two optimisation advances will be explored in the present work, followed by a discussion on advancing nonlinear mod-

[1]OB, Leeds Institute of Fluid Dynamics, University of Leeds, LS2 9JT, Leeds, UK o.bokhove@leeds.ac.uk

[2]HT, School of Mechanical Engineering, University of Leeds, LS2 9JT, Leeds, UK h.m.thompson@leeds.ac.uk

elling of the wave dynamics:

- A theoretical formulation and exploration will be given of the tubular generator by comparing the models with one and three induction coils of the same length (§II). Tubular generators have several advantages (direct conversion) and disadvantages (requiring robust ball-bearings for motion guidance), for a discussion see [4], [16].
- The width and angles of the linear buoy and contraction geometry will be optimised using (Design-of-Experiment and Latin-hypercube-sampling) calculations based on linear finite-element modelling of the entire device (§III). An overview of such geometric optimisation is given in [13].
- Potential-flow or Boussinesq-type wave modelling for wave-energy devices will be discussed with a new formulation of the coupled wave and buoy motion using an augmented Lagrangian, see [9], [21] (§IV).

II. WAVE-TO-WIRE MATHEMATICAL MODEL: BUOY AND GNERATOR

While we refer to Bokhove, Kalogirou and Zweers [5] for the full, original derivation of the wave-to-wire model, we will here focus on consequences of an extension in the set-up of the tubular generator with its connection to the buoy motion[1]. The unidirectional motion of the buoy is governed by its vertical position $Z(t)$, its velocity $W(t) = \dot{Z} \equiv dZ/dt$ under gravity with acceleration g downwards, the hydrodynamic force $F(t)$ on its hull and the forces due to the electromagnetic drag. The buoy with its mast and magnet has mass M and is constrained to move vertically[2].

The extension consists of replacing the single induction coil of length L with three induction coils each of length $L/3$ with reoriented winding configurations followed by an (ideal) full-phase AC-DC full-bridge rectifier for each coil. Each rectifier takes care that the alternating current I_i in coil i becomes a DC-current $|I_i|$ with $i = 1, 2, 3$, which set-up is somewhat related to work in [3]. The length L_m of the single magnet stays the same. Those DC currents in the model are directly used in a Shockley equation representing energy-consuming LED loads since the coils are mathematically connected in parallel via the Shockley equation. Each induction circuit has charge $I_i = \dot{Q}_i$ with the dot denoting a time derivative.

Consequently, the coupled dynamics of the buoy and tubular motor with a single magnet moving through the three induction coils consists of eight ordinary differential equations, as follows

$$\dot{Z} = W, \tag{1a}$$

$$M\dot{W} = -Mg - 2\pi a \sum_{i=1}^{3} \varepsilon_I^{(i)}(Z)I_i + F, \tag{1b}$$

$$\dot{Q}_i = I_i, \tag{1c}$$

$$L_i^{(i)}\dot{I}_i = 2\pi a \varepsilon_I^{(i)}(Z)\dot{Z} - (R_i^{(i)} + R_c^{(i)})I_i$$
$$\qquad - \frac{I_i}{|I_i|}V_S(|I_1| + |I_2| + |I_3|) \tag{1d}$$

for $i = 1, 2, 3$, with coil densities $\varepsilon_I^{(i)}(Z)$ (see below), a Shockley equation

$$V_S(|I|) = n_q V_T \ln\left(1 + |I|/I_{sat}\right)$$
$$\qquad \text{with } |I| = |I_1| + |I_2| + |I_3|, \tag{1e}$$

n_q a quality factor, V_T a thermal voltage and I_{sat} a saturation current. The energy is consumed in loads modelled by a Shockley equation after these AC-DC rectifications. The load is partitioned mathematically into each equation via the overall rectified current $|I| = |I_1| + |I_2| + |I_3|$, which is argued to be the case by the following argument, supported by the circuit diagram in Fig. 2.
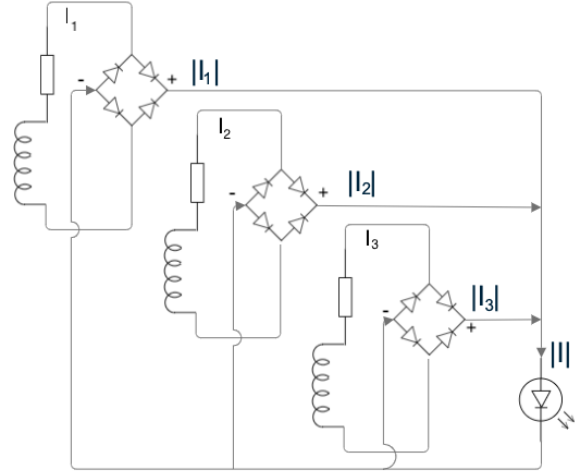

Fig. 2: Circuit schematic of three induction coils, each with inductance $L_i^{(i)} = L_i/3$, resistance of induction coil and its circuit $R_c^{(i)} + R_i^{(i)} = (R_c + R_i)/3$, in which each AC-current I_i is rectified to a DC current $|I_i|$ for $i = 1, 2, 3$, and connected in parallel to a Shockley load, pictured as light-emitting LED.

Consider the case where I_1, I_2, I_3 all have the same signs, then the voltage drop V_s is the same for each induction equation and V_s has $I = |I_1 + I_2 + I_3|$ as argument. Similar checks can be made for the other, different sign configurations. Kirhchoff's circulation laws have been used to formulate the equations for the three parallel circuits involving each inductor, the Lenz' effect and the resistance of the coils and connections. The Lenz' effect enters as the forces proportional to the currents I_i in the momentum equation (1b) and via the terms proportional to $\dot{Z}$ in the current

---

[1]We are particularly building on the model derivation of a tubular generator with a single magnet and single induction coil in the Appendix of Bokhove, Kalogirou and Zweers [5]. However, we do note that the complete model is given here in the combined equation sets (1) and (18).

[2]Parameters and values/ranges used are found in Table I.

equations(1d). Multiplication of these equations by W and I_i shows that these transfer terms $\varepsilon_I^{(i)}(Z)I_i$ cancel after adding the relevant "kinetic" energy terms. The coil densities are nonlinear functions of buoy position Z and are approximately given by a modification of expression (44e) in [5], i.e. they take the forms

$$\varepsilon_I^{(1)}(Z) = \frac{a\mu N}{L}\left(\frac{1}{(a^2+(\bar{Z}+\alpha_h H_m - Z - L/2)^2)^{3/2}}\right.$$
$$\left. -\frac{1}{(a^2+(\bar{Z}+\alpha_h H_m - Z - L/6)^2)^{3/2}}\right) \quad (2a)$$

$$\varepsilon_I^{(2)}(Z) = \frac{a\mu N}{L}\left(\frac{1}{(a^2+(\bar{Z}+\alpha_h H_m - Z - L/6)^2)^{3/2}}\right.$$
$$\left. -\frac{1}{(a^2+(\bar{Z}+\alpha_h H_m - Z + L/6)^2)^{3/2}}\right) \quad (2b)$$

$$\varepsilon_I^{(3)}(Z) = \frac{a\mu N}{L}\left(\frac{1}{(a^2+(\bar{Z}+\alpha_h H_m - Z + L/6)^2)^{3/2}}\right.$$
$$\left. -\frac{1}{(a^2+(\bar{Z}+\alpha_h H_m - Z + L/2)^2)^{3/2}}\right) \quad (2c)$$

for the three coils located after a centering shift at $[-L/2, L/6]$, $[-L/6, L/6]$ and $[L/6, L/2]$ instead of one coil located after this shift at $[-L/2, L/2]$. The single coil has N windings, radius a and length L, while the shorter coils each have $N/3$ windings and length $L/3$. The distance above the reference buoy position Z is $\alpha_h H_m$ and the rest level position of the buoy is $\bar{Z}$, with $\alpha \in [0,1]$.

TABLE I: Table with symbols, units and parameter values or ranges used throughout this paper.

Parameter	symbol	unit	value
tank width	L_x	m	[0.2, 0.55]
rest free-surface depth	H_0	m	[0.075, 0.15]
mass buoy	M	kg	0.08
mast length	H_m	m	0.2
one-coil length	L	m	0.025
current	I	A	
coil diameter	D	mm	0.2769
coil outer radius	a	m	0.012
winding layers	n_{li}	-	10
coil windings	$N = n_{li}L/D$	-	(2889)
magnetic dipole mom.	m	Am^2	5
magnet radius	A_m	m	0.0075
magnet length	L_m	m	0.025
scale factor	α_h	-	0.05
permeability	μ_0	H/m	$4\pi 10^{-7}$
magnetic flux	$\mu = \mu_0 m/(4\pi)$	Nm/A	
quality factor	K	-	0.53
coil induction	$L_i = K\pi a^2 \mu_0 N^2/L$	NM/A^2	0.0099
conductivity	σ	A/VM	5.96×10^7
resistance coil	$R_c = 8aN/(\sigma D^2)$	V/A	18.97
resistance coil circuit	$R_i = R_c$	V/A	18.97
saturation current	I_{sat}	A	0.02
thermal voltage	V_T	V	2.05
Shockley quality factor	n_q	-	0.1
lin. Shockley resistance	$R_l = n_q V_T/I_{sat}$	V/A	102.5
acceleration of gravity	g	m/s^2	9.81

Each induction coil with its rectifier acts as a "battery" unit. When these three units instead are placed in series there is only a single AC current I and DC (rectified) current $|I|$.

Hence, the overall formulation of the three coils reduces to the single coil formulation, as follows

$$(L_i^{(1)} + L_i^{(2)} + L_i^{(3)})\dot{I} = 2\pi a(\varepsilon_I^{(1)} + \varepsilon_I^{(2)} + \varepsilon_I^{(3)})\dot{Z}$$
$$- (R_c^{(1)} + R_c^{(2)} + R_c^{(3)} + R_i^{(1)} + R_i^{(2)} + R_i^{(3)})I - \text{sign}(I)V_s(|I|)$$
$$\Longleftrightarrow L_i\dot{I} = 2\pi a\varepsilon_i(Z)\dot{Z} - (R_c + R_i)I - \text{sign}(I)V_s(|I|), \quad (3)$$

since $L_i^{(i)} = L_i/3, R_c^{(i)} \geq R_c/3, R_i^{(i)} = R_i/3$ (the equal signs hold for ideal, non-dissipative rectifiers), and $\sum_{i=1}^{3}\varepsilon_i^{(i)}(Z) = \varepsilon_I(Z)$, for the latter which see Fig. 3. Instead, we have explored the placement of the three AC-circuits in parallel after rectification and its altered formulation (1).
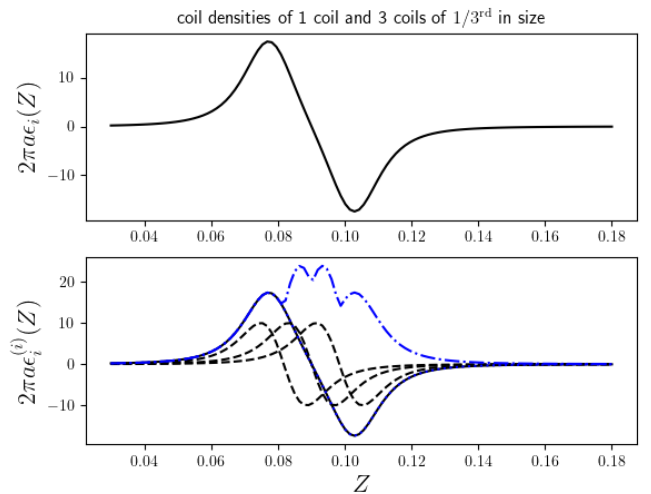

Fig. 3: Coil densities (times $2\pi a$) for a single coil and three coils $1/3^{\text{rd}}$ in size. The top panel is similar to the one in [7]. In the bottom panel, the coil densities of the three separate coils are shown as dashed lines, their sum corresponds to the one-coil case and the sum of their absolute values to the dashed-dotted blue line, which shape emerges later in the power produced.

A. Resonance and Forced-Dissipative Analysis

The linearised coupled buoy-generator subsystem with one coil reads:

$$\dot{Z} = W, \quad (4a)$$
$$M\dot{W} = -\gamma G(Z_0)I + F(t), \quad (4b)$$
$$\dot{Q} = I, \quad (4c)$$
$$L_i\dot{I} = \gamma G(Z_0)\dot{Z} - (R_c + R_i + R_l)I - \frac{Q}{C}, \quad (4d)$$

in which we have added a capacitor C to the Shockley load with its linearised resistance R_l and in which the hydrodynamic forcing in the buoy's momentum equation is simplified to a prescribed force $F(t)$. The coil density $2\pi a\varepsilon(Z) \equiv \gamma G(Z)$ with $\gamma = 2\pi\mu a^2/L$ is evaluated at the rest level Z_0 of the buoy in the linearisation. The other variables have been linearised around their zero rest state. In the absence of forcing $F(t) = 0$

and dissipation $R_c = R_i = R_l = 0$, this subsystem of coupled oscillators has eigenfrequencies

$$\omega_i^2 = 0, \omega_i = \pm\sqrt{(L_i)^{-1}}\sqrt{1/C + \gamma^2 G(Z_0)^2/M} \quad (5)$$

with limiting cases $1/C \to 0$ and $\gamma \to 0$, in the latter which case $\omega_i \to \pm\sqrt{(L_iC)^{-1}}$. Hence, larger values of L_i, C, M reduce the eigenfrequency ω_i and larger values of $\gamma G(Z_0)$ and inverse capacitance $1/C$ increase the eigenfrequency. Regardless, adding a capacitor increases the eigenfrequency. Given that $\gamma = 2\pi a^2 \mu N/L$ and $L_i = K\mu_0(N^2/L)\pi a^2$ ([5], [7]), it is best to look at the combination $\gamma^2 G(Z_0)^2/L_i$.

Next we analyse the subsystem (4) under harmonic forcing. Given that $F(t) \propto e^{i\sigma t}$, we posit solutions of the form

$$\begin{pmatrix} Z(t) \\ W(t) \\ I(t) \\ Q(t) \end{pmatrix} = \mathrm{Re}\left\{\mathbf{x}e^{i\sigma t}\right\} \equiv \mathrm{Re}\left\{\begin{pmatrix} \hat{Z} \\ \hat{W} \\ \hat{I} \\ \hat{Q} \end{pmatrix} e^{i\sigma t}\right\},$$

such that, upon division by $e^{i\sigma t}$, system (4) can be written in matrix form as $\mathbf{Ax} = \mathbf{b}$, where

$$\mathbf{A} = \begin{pmatrix} i\sigma & -1 & 0 & 0 \\ 0 & iM\sigma & \gamma G & 0 \\ 0 & 0 & -1 & i\sigma \\ -i\gamma G\sigma & 0 & iL_i\sigma + R & \frac{1}{C} \end{pmatrix}$$

with $G \equiv G(Z_0)$ and $R \equiv R_c + R_i + R_l$, and

$$\mathbf{b} = (0, A_r + iA_i, 0, 0)^T.$$

By inverting matrix $\mathbf{A}$, using Python's `sympy` package, the solution $\mathbf{x} = \mathbf{A}^{-1}\mathbf{b}$ is

$$\begin{pmatrix} \hat{Z} \\ \hat{W} \\ \hat{I} \\ \hat{Q} \end{pmatrix} = \begin{pmatrix} \dfrac{(A_r + iA_i)\left(CL_i\sigma^2 - iCR\sigma - 1\right)}{\sigma^2\left(CG^2\gamma^2 - CL_iM\sigma^2 + iCMR\sigma + M\right)} \\[2ex] \dfrac{i(A_r + iA_i)\left(CL_i\sigma^2 - iCR\sigma - 1\right)}{\sigma\left(CG^2\gamma^2 - CL_iM\sigma^2 + iCMR\sigma + M\right)} \\[2ex] \dfrac{CG\gamma(A_r + iA_i)}{CG^2\gamma^2 - CL_iM\sigma^2 + iCMR\sigma + M} \\[2ex] \dfrac{CG\gamma(A_i - iA_r)}{\sigma(CG^2\gamma^2 - CL_iM\sigma^2 + iCMR\sigma + M)} \end{pmatrix}. \quad (6)$$

Solutions to system (4) can be found by taking the real and imaginary parts of (6) separately, and multiplying by $\cos\sigma t$ and $-\sin\sigma t$ respectively, i.e.

$$I = \mathrm{Re}\{\hat{I}\}\cos\sigma t - \mathrm{Im}\{\hat{I}\}\sin\sigma t$$
$$\text{and} \quad Q = \mathrm{Re}\{\hat{Q}\}\cos\sigma t - \mathrm{Im}\{\hat{Q}\}\sin\sigma t. \quad (7)$$

To calculate the power, we do not require expressions for Z and W. Using (7), we can explicitly evaluate the average power output, with $T = n\pi/\sigma$:

$$\hat{P}_g = \frac{1}{T}\int_0^T I^2 R_l + \frac{IQ}{C}dt = \frac{1}{2}\Big(R_l\left(\mathrm{Re}\{\hat{I}\}^2 + \mathrm{Im}\{\hat{I}\}^2\right) + \frac{1}{C}\left(\mathrm{Re}\{\hat{I}\}\mathrm{Re}\{\hat{Q}\} + \mathrm{Im}\{\hat{I}\}\mathrm{Im}\{\hat{Q}\}\right)\Big), \quad (8)$$

since $\int_0^{n\pi/\sigma}\cos^2\sigma t\,dt = \int_0^{n\pi/\sigma}\sin^2\sigma t\,dt = n\pi/(2\sigma)$ and $\int_0^{n\pi/\sigma}\cos\sigma t\sin\sigma t = 0$. Using (7) in (4c) yields that

$$\mathrm{Re}\{\hat{Q}\} = \mathrm{Im}\{\hat{I}\}/\sigma \text{ and } \mathrm{Im}\{\hat{Q}\} = -\mathrm{Re}\{\hat{I}\}/\sigma.$$

Hence, $\mathrm{Re}\{\hat{I}\}\mathrm{Re}\{\hat{Q}\} + \mathrm{Im}\{\hat{I}\}\mathrm{Im}\{\hat{Q}\} = 0$, such that the second term of (8) can be removed, giving

$$\hat{P}_g = \frac{1}{2}R_l\left(\mathrm{Re}\{\hat{I}\}^2 + \mathrm{Im}\{\hat{I}\}^2\right).$$

With $CG^2\gamma^2 - CL_iM\sigma^2 + M = \alpha_0$ and $CMR\sigma = \alpha_1$, we find

$$\hat{I} = \frac{CG\gamma(A_r + iA_i)}{\alpha + i\beta} = \frac{CG\gamma(A_r + iA_i)(\alpha_0 - i\alpha_1)}{\alpha_0^2 + \alpha_1^2}$$
$$\Rightarrow (\mathrm{Re}\{\hat{I}\}, \mathrm{Im}\{\hat{I}\}) = CG\gamma\frac{((A_r\alpha_0 + A_i\alpha_1), A_i\alpha_0 - A_r\alpha_1))}{\alpha_0^2 + \alpha_1^2},$$

such that

$$\hat{P}_g = \frac{R_lC^2G^2\gamma^2}{2\left(\alpha_0^2 + \alpha_1^2\right)^2}\left((A_r\alpha_0 + A_i\alpha_1)^2 + (A_i\alpha_0 - A_r\alpha_1)^2\right)$$
$$= \frac{R_lC^2G^2\gamma^2(A_r^2 + A_i^2)}{2\left(\alpha_0^2 + \alpha_1^2\right)}.$$

Substituting for α_0 and α_1 as well as dividing top and bottom by C^2, the final power output becomes

$$\hat{P}_g = \frac{1}{2}\frac{R_lG^2\gamma^2(A_r^2 + A_i^2)}{\left(G^2\gamma^2 - L_iM\sigma^2 + M/C\right)^2 + (MR\sigma)^2}. \quad (9)$$

For $C \to \infty$, total power generated and lost thus read

$$\hat{P}_g = \frac{1}{2}\frac{R_lG^2\gamma^2(A_r^2 + A_i^2)}{\left(G^2\gamma^2 - L_iM\sigma^2\right)^2 + (MR\sigma)^2}, \quad (10a)$$
$$\hat{P}_l = \frac{1}{2}\frac{(R_c + R_i)G^2\gamma^2(A_r^2 + A_i^2)}{\left(G^2\gamma^2 - L_iM\sigma^2\right)^2 + (MR\sigma)^2}. \quad (10b)$$

At the resonance frequency $\gamma G(Z_0)/\sqrt{ML_i} \sim 0.2673$Hz (e.g. with $\gamma = 3.66 \times 10^{-6}, M = 0.1, L_i = 0.35, R_l = 102, R_i = R_c = 203, \gamma G(Z_0) = 0.05$) the power output is

$$\hat{P}_g = \frac{1}{2}R_lL_i(A_r^2 + A_i^2)/(MR^2). \quad (11)$$

Therefore, with $R_l \approx 102$ and $A_r + iA_i = A$, one finds that $P \approx 7 \times 10^{-4}|A|^2 = 2.8 \times 10^{-7}$J for $A = 0.02$.

When $1/C = 0$, $L_iM\sigma^2 > \gamma^2G^2$ and for given σ, this linear resonance can be reached if and only if

$$C = M1/(L_iM\sigma^2 - \gamma^2G^2), \quad (12)$$

and can be enforced at the level

$$\hat{P}_g = \frac{1}{2}R_l\gamma^2G^2)L_i(A_r^2 + A_i^2)/(MR^2\sigma^2), \quad (13)$$

as a controller. For the values used above and the forcing frequency $\sigma = 9.34\text{s}^{-1}$ numerically found for the full yet linearised system in Bolton, Bokhove, Borman, Kalogirou and Thompson [7], we then calculate that $C = 0.0328$F.
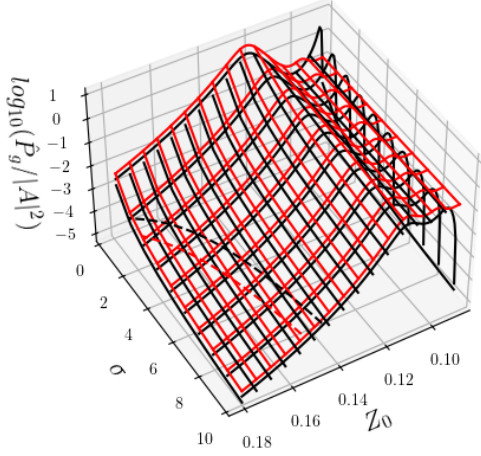
Fig. 4: Power output over amplitude $P_g/|A|^2$ as function of (modelled hydrodynamic) forcing frequency σ and buoy rest level Z_0 for single coil (black lines) and three-coils-in-parallel (red lines) cases, with full-wave rectifiers for each case. Resonant cases are displayed with dashed lines. Half of the profile is shown.
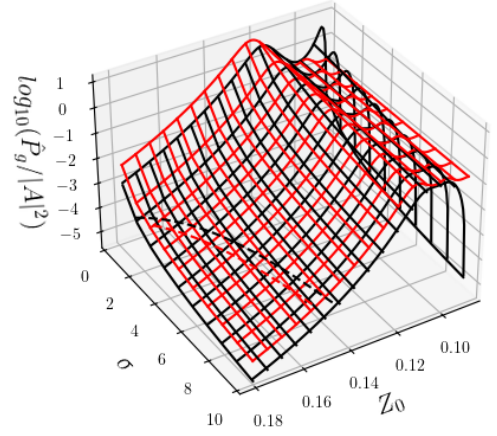

Fig. 5: Power output over amplitude $P_g/|A|^2$ as function of forcing frequency σ and buoy rest level Z_0 for single coil (black lines) and three-coils-in-parallel (red lines) cases, with full-wave rectifiers for each case. Resonant case displayed with dashed lines. Here we took $R_l \to 3R_l, R \to R_c + R_i + 3R_l$ in the single-coil case.

Similarly, the linearised forced-dissipative three-coil case connected in parallel after rectification involves eight equations, i.e. for $\{Z, W, I_1, Q_1, I_2, Q_2, I_3, Q_3\}$, and is approximated as follows

$$\dot{Z} = W, \tag{14a}$$

$$M\dot{W} = -\gamma G(Z_0)I + F(t), \tag{14b}$$

$$\dot{Q}_i = I_i, \tag{14c}$$

$$L_i\dot{I}_i = \gamma G_i(Z_0)\dot{Z} - (R_c^{(i)} + R_i^{(i)} + R_l)I_i \text{ for } i = 1,2,3, \tag{14d}$$

in which R_l is the full linearised Shockley load, while we recall that $R_c^{(i)} = R_c/3, R_i^{(i)} = R_i/3$. Note that this is an approximation since a Shockley load has been included in each circuit because it is not clear how to linearise $-\text{sign}(I_i)R_l(|I_1| + |I_2| + |I_3|)$. To allow another comparison between the single coil and three-coil cases, we have (also) increased the linearised Shockley load in the single-coil case by a factor of three: $R_l \to 3R_l, R \to R = R_c + R_i + 3R_l$.

Its solution for the currents without capacitor and with $R = R_c/3 + R_i/3 + R_l/3$ reads (again by using Python's `sympy` package)

$$\begin{pmatrix} \hat{I}_1 \\ \hat{I}_2 \\ \hat{I}_3 \end{pmatrix} = \begin{pmatrix} \dfrac{(A_r + iA_i)(3\gamma G_1)}{(3\gamma^2(G_1^2 + G_2^2 + G_3^2) - L_iM\sigma^2 + iMR\omega)} \\ \dfrac{i(A_r + iA_i)(3\gamma G_2)}{(3\gamma^2(G_1^2 + G_2^2 + G_3^2) - L_iM\sigma^2 + iMR\omega)} \\ \dfrac{CG\gamma(A_r + iA_i)(3\gamma G_3)}{(3\gamma^2(G_1^2 + G_2^2 + G_3^2) - L_iM\sigma^2 + iMR\omega)} \end{pmatrix}. \tag{15}$$

Similar analysis as for the one-coil case then yields that the power gained

$$\hat{P}_g = \frac{1}{2} \frac{9R_l\gamma^2(G_1^2 + G_2^2 + G_3^2)(A_r^2 + A_i^2)}{\left(3\gamma^2(G_1^2 + G_2^2 + G_3^2) - L_iM\sigma^2\right)^2 + (MR\sigma)^2}, \tag{16}$$

from which we see that the free-wave resonant frequency is

$$\omega_i = 3\gamma\sqrt{(G_1^2 + G_2^2 + G_3^2)}/(\sqrt{M}L_i). \tag{17}$$

The power output for both the single coil and three-coil-in-parallel cases are displayed in Fig. 4 with solid black and red lines respectively as function of forcing frequency σ and (rest or linearisation) buoy level Z_0. The three-coil-in-parallel case reaches a higher output of circa half a decade away from Z_0 with single-coil $G(Z_0) = 0$. Near that point and for smaller σ the single-coil case is more effective. However, this difference is a bit artificial due to the associated linearisation process in that in reality Z marches through a range of values. Note that at resonance, the achievable maximally gained power is the same (11) between the one-coil and three-coil cases, as displayed with the dashed lines in Figs. 4 and 5. At least in the single-coil case, the effect of the capacitor control is minimal, since for $L_iM\sigma^2 > \gamma^2G^2$ the term $(MR\sigma)^2$ dominates.

Of course, nonlinear effects will lead to some averaging over Z. A weakly nonlinear analysis or fully nonlinear numerical simulation will be required to assess the nonlinear effects of the coil densities and Shockley load.
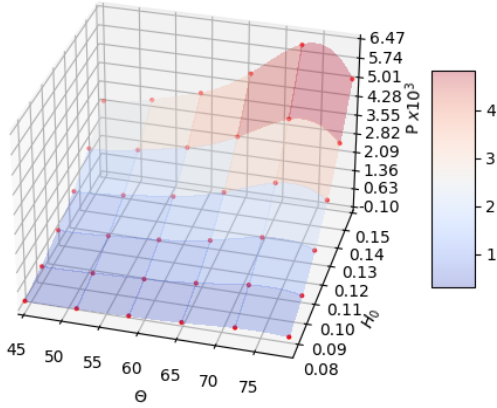
Fig. 6: Power output over 36 simulations with varying $\theta_c \in [45, 80]^o$, $H_0 \in [0.075, 0.15]$m, while keeping $L_x = 0.2$m and other parameters fixed.
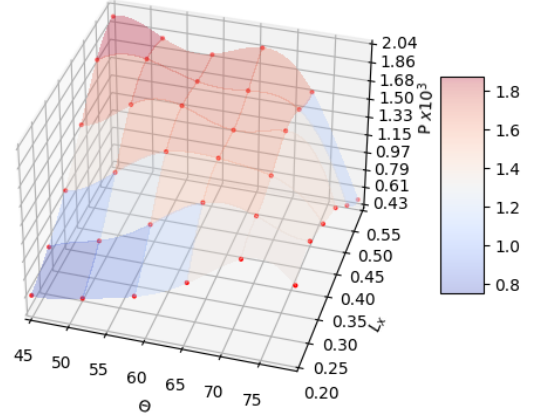

Fig. 7: Power output over 36 simulations with varying $\theta_c \in [45, 80]^o$, $L_x \in [0.2, 0.55]$m, while keeping $H_0 = 0.1$m and other parameters fixed.

III. DESIGN-OF-EXPERIMENT: SAMPLING CONTRACTION GEOMETRIES

Hitherto we have chosen linear contraction and buoy geometries. The shape of the buoy is therefore a prism. The following three parameters determine contraction and buoy shapes: the width L_x of the contraction entrance, the angle $\theta = \theta_c$ of the contraction wall with the wall normal and the angle α of the buoy hull. Simulations of the linear shallow water finite-element model coupled to the buoy and then to the generator with loads will be used to calculate the power output for a series of parameter values. For details, we refer to [7] for our numerical set-up, which finite-element discretisation is fully compatible and includes two-way coupling between hydrodynamics and buoy motion as well as buoy motion and power generation[3]. Since a full sweep of simulations across a renewed set of parameter values over a regular grid pattern is computationally expensive, we also explore the use of surrogate modelling to lower the computational efforts. The goal is to find the parameter values that optimise the power output in order to aid in the design of the laboratory experiment.

Here, we focus on the parameter plane spanned by θ_c and L_x or H_0 for incoming monochromatic waves, generated by a piston wavemaker for our laboratory-size tank. Several sets of simulations will be undertaken. For $L_x = 0.2$m we will calculate and display the power output for 36 values value-pairings within parameter ranges $\theta_c \in [45, 80]^o$, $H_0 \in [0.075, 0.15]$m. Subsequently, for $H_0 = 0.1$m, simulations will be run for 36 suitable (random-covering) value-pairings within parameter ranges $\theta_c \in [45, 80]^o$, $L_x \in [0.2, 0.55]$m. Optimisation values are also gathered using Latin-hypercube sampling as routinely used in Design-of-Experiments (DOE).

---

[3]Access to a bespoke GitHub repository is available upon request.

Given these outcomes for the power output, Gaussian Radial Basis Functions will be used to find an overall fit, whereupon the maximum output will be determined. It turns out that a fitting with Gaussian processes leads to unphysical negative power outputs so we rejected this Gaussian choice of surrogate modelling.

The simulation sweep over θ_c and H_0 is displayed in Fig. 6 revealing a maximum power output of circa $\theta_c = 74^o$ for all $H_0 \in [0.075, 0.15]$m. Simulations displayed in Fig. 7 (and surrogate modelling) reveal maximum values around a plateau bounded by lines connecting points $[74^o, 0.2m], [45^o, 0.55m]$ and $[74^o, 0.2m], [65^o, 0.55m]$ within the range $[\theta_c, L_x] = [45, 80]^o \times [0.2, 0.55]$m investigated. Naturally, the power increases uniformly as function of H_0 since the piston wavemaker displacement stayed the same so more water is moved for larger H_0. Power should perhaps increase (linearly) with L_x which is, however, only seen for $\theta_c \in [45]^o$, but there may be insufficient resolution within the contraction for large angle $\theta_c \approx 80^o$.

IV. DISCUSSION: INEQUALITY CONSTRAINT VIA AUGMENTED LAGRANGIAN

We have explored two optimisation options to enhance the power output in our wave-energy device, which consists of a wave-amplifying contraction and a floating buoy with magnet moving in a (predominantly) vertical direction which is coupled to a tubular electromagnetic generator.

First, the model of the original single-magnet and single-coil generator has been replaced by one with a single-magnet and three-coils-in-parallel generator. Together the three induction coils have the same length and properties as the single induction coil. The power output is mostly about an order of magnitude larger in the three-coil case, which is revealed in an analysis of the separate buoy-generator

dynamics after linearisation of the nonlinear model around a rest state and with hypothetical harmonic (hydrodynamic) forcing. Power output is magnitudes larger when the rest level is (mis)placed near the middle of the coils but herein the linearisation may be misleading. Full numerical simulations or weakly nonlinear analysis of the nonlinear (sub)system of the device are required to further understanding. We aim to build the subsystem for experimental model validation.

Second, the linear contraction geometry has been optimised based on (Latin-hypercube) simulations of a simplified and linearised complete wave-to-wire model. A model reduction from dispersive potential-flow hydrodynamics equations to the shallow-water equations was made as well as linearisation of the wave-to-wire model. Based on the laboratory tank dimensions, power-output maxima were obtained for the following tank width and contraction angle: $L_x = 0.2$m and $\theta \approx 74^0$ independent of depth $H_0 \in [0.075, 0.15]$m. Based on these preliminary results we aim to make a first laboratory realisation in our available wavetank.

The optimisation explorations have hitherto been limited to linearised versions of the complete nonlinear models. Instead of using Navier-Stokes equations for the hydrodynamics, we favour the use of potential-flow and Boussinesq-type dispersive wave models ([17], [15]). For nonlinear wave modelling, these models are computationally much faster than the Navier-Stokes equations and well-explored in the wave-modelling applied-mathematics community. For numerical wave modelling, e.g., we refer to boundary/finite-element models of Ma et al. [19], Engsig-Karup, Bingham [11] and Boussinesq models [18], the latter which use optimised and reduced vertical resolution (for other variational models see [14], [15], [10]). Typically, second or higher-order time discretisations are used such as compatible modified midpoint ([8], [10]) or Runge-Kutta schemes. A crucial aspect is the coupling to the buoy in the wave-energy device. A fully nonlinear model was formulated in Bokhove, Kalogirou and Zweers [5] in which the pressure under the wetted hull acted as a Lagrange multiplier $\tilde{\lambda} \geq 0$, wherein $\tilde{\lambda} = 0$ at the waterline. This moving waterline was resolved exactly and implicitly where the water depth $z = h(x,y,t)$ equals the position of the buoy hull $z = h_b(Z(t), x, y)$ over a flat bottom at vertical position $z = 0$. Hence, the waterline is defined by equality constraint $h(x,y,t) - h_b(Z(t), x, y) = 0$ with horizontal coordinates x and y and buoy location $Z(t)$. In h_b various parameters describing the fixed buoy shape have been suppressed. This exact (numerical) modelling is complicated, requiring meshes conforming to the dynamic waterline. Therefore, we next outline a model formulation based on inequality constraints $h(x,y,t) - h_b(Z(t), x, y) \leq 0$, cf. developments and results of contact dynamics in continuum mechanics [9].

Consider our wavetank with a piston wavemaker at $x = R_w(t)$ and a contraction. Its domain is $x \in [0, L_x], y \in [R_w(t), l_y(x)]$ with $l_y(x) = L_y - L_c|1 - 2x/L_x|$ and L_c the contraction length at the tank's centreline; furthermore $z \in [0, h(x,y,t)]$. At rest the free-surface water level in the tank is H_0 and under the buoy it is determined

by Archimedes principle. For an incompressible fluid of constant density and three-dimensional velocity $\mathbf{u} = \nabla\phi$, the interior fluid is governed by the Laplace equation

$$\nabla^2 \phi = 0 \qquad (18\text{a})$$

for the velocity potential $\phi(x,y,z,t)$. The time dependence is governed by the kinematic and Bernoulli equations at the free surface $z = h(x,y,t)$ of the water

$$\partial_t \phi + \frac{1}{2}|\nabla\phi|^2 + g(h - H_0) + F_+ \left(\gamma_n(h - h_b) - \lambda\right) = 0, \qquad (18\text{b})$$

$$\partial_t h + \nabla\phi \cdot \nabla h = \partial_z \phi, \qquad (18\text{c})$$

coupled to the buoy motion via an added inequality constraint-force

$$MW = -Mg - 2\pi a \sum_{i=1}^{3} \varepsilon_I^{(i)}(Z) I_i$$
$$- \int_0^{L_x} \int_0^{l_y(x)} F_+ \left(\gamma_n(h - h_b) - \lambda\right) \mathrm{d}x\,\mathrm{d}y, \qquad (18\text{d})$$

and with notation $\partial_t h \equiv \partial h/\partial t, \partial_z \phi \equiv \partial\phi/\partial z, \nabla \equiv (\partial_x, \partial_y, \partial_z)^T$. The function $F_+(q) = \max(q,0)$, or a smooth approximation thereof, and the Lagrange multiplier $\lambda(x,y,t)$ under the hull is the (negative) hydrodynamic pressure on the hull such that $\lambda \leq 0$ (N.B. $\tilde{\lambda} \propto -\lambda$). This Lagrange multiplier is governed by the equation

$$\lambda = -F_+ \left(\gamma_n(h - h_b) - \lambda\right), \qquad (18\text{e})$$

with constant $\gamma_n \gg 0$. After some manipulation, one can show that (18e) for $F_+(q) = \max(q,0)$ satisfies the well-known Karush-Kuhn-Tucker inequality conditions

$$h - h_b \leq 0, \quad \lambda \leq 0, \quad \lambda(h - h_b) = 0. \qquad (19)$$

So either $\lambda = 0$ or $h = h_b$. Moreover, the Lagrange multiplier equation (18e) and in fact the entire (conservative part of the) system can be derived from an augmented Lagrangian formulation (by combining the work in [5], [9], [21]), which aids both numerical formulation and implementation.

The numerical implementation of such fully nonlinear wave-to-wire models using this inequality constrained formulation is in progress within the finite-element environment `Firedrake` ([22], [1], [2], [21]). That environment in particular lends itself for the implementation of the (time-discrete) variational principle or augmented Lagrangian underlying the entire wave-to-wire model. Therein algebraically-complicated weak formulations can be generated automatically and the dissipative features can furthermore readily be added to these conservative parts.

REFERENCES

[1] M.S. Alnaes, UFL: a finite element form language. In: Automated Solution of Differential Equations by the Finite Element Method. Eds: A. Logg and K.-A. Mardal and G. N. Wells, Springer, Berlin. 2011.

[2] M.S. Alnaes, A. Logg, K.B. Oelgaard, M.E. Rognes, G.N. Wells G.N., Unified Form Language: A domain-specific language for weak formulations of partial differential equations. 2013. `https://arxiv.org/pdf/1211.4047.pdf`

[3] M. Baumann, J.W. Kolnar, Parallel connection of two three-phase three-switch buck-type unity-power-factor rectifier systems with DC-link current balancing. IEEE Trans. Industrial Electronics 54, 2007, 3042.

[4] N. Bianchi, S. Bolognano, D.D. Corte, F. Tonel, Tubular linear permanent magnet motors: an overall comparison. IEEE Trans. Industrial Applications 39(2), 2003, 0093-9994.

[5] O. Bokhove, A. Kalogirou, W. Zweers, From bore-soliton-splash to a new wave-to-wire wave-energy model. Water Waves 1(2), 2019, 217–258. For the movie of the man-made rogue wave, see: `https://www.youtube.com/watch?v=YSXsXNX4zW0`

[6] O. Bokhove, A. Kalogirou, D. Henry, G. Thomas, A novel rogue-wave-energy device with wave amplification and induction actuator. Int. Marine Energy Journal 30, 2020, 37–43.

[7] J. Bolton, O.Bokhove, D. Borman, A. Kalogirou, H. Thompson, Towards optimization of a wave-to-wire energy device in a breakwater contraction. European Wave and Tidal Energy Conf., Plymouth, 2021 10 pp. `https://tethys-engineering.pnnl.gov/sites/default/files/publications/2191.pdf`

[8] J.D. Brown, Midpoint rule as a variational-symplectic integrator: Hamiltonian systems. Physical Review D 73, 2006, 2400.

[9] E. Burman, P. Hansbo, M.G. Larson, The augmented Lagrangian method as a framework for stabilised methods in computational mechanics. Archives of Computational Methods in Engineering 30, 2023, 2579—2604.

[10] J. Choi, A. Kalogirou, A., Y. Lu, O. Bokhove, M. Kelmanson, A study of extreme water waves using a hierarchy of models based on potential-flow theory, Water Waves, 2024, online.

[11] A.P. Engsig-Karup, H.B. Bingham, O. Lindberg, An efficient flexible-order model for 3D nonlinear water waves, J. Comp. Phys. 228, 2009, 2100–2118.

[12] A.F.O. Falcäo, Wave energy utilization: a review of the technologies. Renew. Sustain. Energy Rev. 14, 2010, 899—918.

[13] A. Garcia Teruel, D.R. Forehand, Review of geometry optimisation of wave energy converters. Renewable and Sustainable Energy Reviews 139, 2021, 110593.

[14] E. Gagarina, Variational approaches to water wave simulations. PhD Thesis, University of Twente, 2014. `https://ris.utwente.nl/ws/portalfiles/portal/6031258/thesis_E_Gagarina.pdf`

[15] F. Gidel, O. Bokhove, A. Kalogirou, Variational modelling of extreme waves through oblique interaction of solitary waves: application to Mach reflection. Nonlinear Proc. Geophys. 24, 2017, 43–60.

[16] P. Khatri, X. Wang, Comprehensive review of a linear electrical generator for ocean wave energy conversion. IET Renewable Power Generation 14, 2020, 949–958.

[17] B.B. Kadomtsev, V.I. Petviashvili, The stability of solitary waves in weakly dispersive media. Dokl. Akad. Nauk SSSR 192, 1970, 532–541.

[18] C. Lawrence, D. Adyttia, E. van Groesen, Variational Boussinesq model for strongly nonlinear dispersive waves. Wave Motion 76, 2018, 78–102.

[19] Q.W. Ma, G.X. Wu, R. Eatock Taylor, Finite element simulation of fully non-linear interaction between vertical cylinders and steep waves. Part 1: methodology and numerical procedure. Int. J. Numerical Methods in Fluids 36, 2001, 265–285.

[20] F. Madhi, R.W. Yeung, On survivability of asymmetric wave-energy converters in extreme waves. Renew. Energy 119, 2018, 891—909.

[21] S. Balay, et al., PETSc, Toolkit for Advanced Optimisation: optimisation solvers, bound-constraint optimisation. 2023.

[22] F. Rathgeber et al., Firedrake: automating the finite element method by composing abstractions. ACM Trans. Math. Softw. 43(3), 2016, 27.

[23] T. Yu, Q. Guo, H. Shi, T. Li, X. Meng, S. He, et al. Experimental investigation of a novel OWC wave energy converter. Ocean Eng. 257, 111567. 2022.